Astronomy & Astrophysics manuscript no. RAPTOR_II_AA
December 4, 2021

RAPTOR II: Polarized radiative transfer in curved spacetime⋆

T. Bronzwaer[1], Z. Younsi[2,3], J. Davelaar[1], H. Falcke[1]

[1] Department of Astrophysics/IMAPP, Radboud University Nijmegen P.O. Box 9010, 6500 GL Nijmegen, The Netherlands
[2] Mullard Space Science Laboratory, University College London, Holmbury St. Mary, Dorking, Surrey, RH5 6NT, United Kingdom
[3] Institut für Theoretische Physik, Goethe-Universität Frankfurt, Max-von-Laue-Straße 1, D-60438 Frankfurt am Main, Germany

December 4, 2021

ABSTRACT

Context. Accreting supermassive black holes are sources of polarized radiation that propagates through highly curved spacetime before reaching the observer. In order to help interpret observations of such polarized emission, accurate and efficient numerical schemes for polarized radiative transfer in curved spacetime are needed.
Aims. In this manuscript we aim to extend our publicly available radiative transfer code RAPTOR (Bronzwaer et al. 2018) to include polarized radiative transfer, so that it can produce simulated polarized observations of accreting black holes. RAPTOR must remain compatible with arbitrary spacetimes, and it must be efficient in operation, despite the added complexity of polarized radiative transfer.
Methods. We provide a brief review of different codes and methods for covariant polarized radiative transfer available in the literature and existing codes, and present an efficient new scheme. For the spacetime-propagation aspect of the computation, we develop a compact, Lorentz-invariant representation of a polarized ray. For the plasma-propagation aspect of the computation, we perform a formal analysis of the stiffness of the polarized radiative-transfer equation with respect to our explicit integrator, and develop a hybrid integration scheme that switches to an implicit integrator in case of stiffness, in order to solve the equation with optimal speed and accuracy for all possible values of the local optical/Faraday thickness of the plasma.
Results. We perform a comprehensive code verification by solving a number of well-known test problems using RAPTOR and comparing its output to exact solutions. We also demonstrate convergence with existing polarized radiative-transfer codes in the context of complex astrophysical problems, where we found that the integrated flux densities for all Stokes parameters converged to excellent agreement.
Conclusions. RAPTOR is capable of performing polarized radiative transfer in arbitrary, highly curved spacetimes. This capability is crucial for interpreting polarized observations of accreting black holes, which can yield information about the magnetic-field configuration in such accretion flows. The efficient formalism implemented in RAPTOR is computationally light and conceptually simple. The code is publicly available.

Key words. radiative transfer – black hole physics – polarization

1. Introduction

Many low-luminosity active galactic nuclei (LLAGN) display prominent jets and compact cores that are sources of highly non-thermal continuum radio emission (see, e.g., Heeschen 1970; Wrobel and Heeschen 1991). The observational signatures of the compact cores have been reproduced using models that produce self-absorbed synchrotron emission in the jet (Falcke and Biermann 1995; Falcke et al. 2004) or in a magnetized accretion flow (Narayan et al. (1998); Yuan et al. (2003); Broderick and Loeb (2006); Moscibrodzka et al. (2009); Dexter et al. (2009); see also Falcke et al. (2001)). This radiation is emitted by relativistic electrons gyrating around magnetic field lines. In the optically thin limit, the emission is significantly polarized (Jones and Hardee 1979), an effect that has been observed in higher-luminosity AGN sources (Gabuzda et al. 1996; Gabuzda and Cawthorne 2000; Lyutikov et al. 2005). The polarized emission from an accreting AGN can therefore yield information about the source's magnetic-field morphology, which may be crucial to the evolution of the AGN's accretion flow. The Event Horizon Telescope (EHT) is a worldwide millimeter-wavelength array capable of resolving the black-hole shadow (Goddi et al. 2017; Event Horizon Telescope Collaboration 2019), a characteristic feature of the radio-frequency emission from optically thin AGN at the scale of the event horizon (Falcke et al. 2000; Broderick and Narayan 2006), although it may be obscured or exaggerated in certain accretion scenarios (see Gralla et al. (2019) and Narayan et al. (2019)). The EHT can also determine the polarization state of such emission: Johnson et al. (2015) reports 1.3-mm observations (230 GHz) that indicate partially ordered magnetic fields within a region of about 6 Schwarzschild radii around the event horizon of Sagittarius A* (Sgr A*), the supermassive black hole in the center of the Milky Way. Bower et al. (2003) report stable long-term behavior and short-term variability in Sgr A* rotation measure, implying a complex inner region (within 10 Schwarzschild radii) in which both emission and propagation effects are important to the observed polarization. Hada et al. (2016) study the central black hole in the galaxy M87, observing a bright feature with (linear) polarization degree of 0.2 at 86 GHz at the jet base. Observations in infrared by Gravity Collaboration (2018) were consistent with a model in which a relativistic 'hot spot' of material, orbiting near Sgr A*'s innermost stable circular orbit (ISCO) in a poloidal magnetic field, emits polarized synchrotron radiation.

To study accreting supermassive black holes, general-relativistic radiative-transfer (GRRT) codes are used (see, e.g.,

⋆ The public version of RAPTOR is available at the following URL: https://github.com/tbronzwaer/raptor

Jaroszynski and Kurpiewski 1997; Bromley et al. 2001; Broderick 2006; Noble et al. 2007; Dexter and Agol 2009; Younsi et al. 2012). GRRT codes solve the geodesic equation in curved spacetime to compute null geodesics, and then solve the radiative-transfer equation along the null geodesics to produce an image. Doing so requires the evaluation of emission and absorption coefficient of radiation along the geodesics. In our case, the emission and absorption coefficients are computed using the state variables of a radiating plasma (the black-hole accretion flow, generally consisting of both a disk and a jet). The plasma variables (such as density, magnetic fields, and temperature) needed to compute the emission and absorption coefficients are either provided by analytical or semi-analytical models, or by fully numerical, general-relativistic magnetohydrodynamical (GRMHD) plasma simulations. Some models, such as the thin-disk model of an accreting black hole in a black-hole binary system (Shakura and Sunyaev (1973) and Novikov and Thorne (1973)), consist of a geometrically thin, optically thick disk, meaning that the emissivity function along a ray is a delta function; other models, such as those based on GRMHD data, may be geometrically thick yet optically thin, necessitating the use of volumetric rendering techniques, specifically, solving the radiative-transfer equation along a ray.

In order to interpret and complement polarized observations, it is important that the numerical radiative-transfer tools used to study accreting supermassive black holes are capable of including polarization. In a previous paper (Bronzwaer et al. 2018), we presented `RAPTOR`, a publicly available GRRT code capable of performing time-dependent radiative transfer in arbitrary spacetimes. In the present paper, we develop a novel formalism and algorithm for polarized radiative transfer in order to extend `RAPTOR`'s capabilities. Two things affect the polarization state of radiation propagating through a plasma in a strong gravitational field, namely: *i*) propagation through curved spacetime itself (which may rotate the polarization vector around the ray's propagation direction), and *ii*) interaction with the plasma (which may affect the polarization state in a general way). In order to model these two processes quantitatively, several equivalent formalisms for covariant polarized radiative transfer have been proposed in the literature; they differ in the ways in which they represent polarized radiation, as well as the method of integration. Broderick and Blandford (2004), Shcherbakov and Huang (2011), Dexter (2016), and Younsi et al. (2020) represent polarized radiation using the Stokes parameters plus a polarization basis vector, integrating the Stokes parameters through curved spacetime and any plasma that may be present while parallel-transporting the basis vector. Moscibrodzka and Gammie (2017) also represents polarized radiation using the Stokes parameters for computing the plasma interaction, but their formalism, which is based on Gammie and Leung (2012), transforms back and forth between the Stokes parameters (which are convenient for computing the ray's interaction with a radiating plasma) and a covariant description of the polarization state, a tensor called the coherence matrix, which is convenient for propagation through spacetime. In this work, we choose to develop a novel formalism for `RAPTOR`, to match with our previously chosen numerical methods (Bronzwaer et al. 2018) and to optimize `RAPTOR`'s computational efficiency and accuracy.

This paper is organized as follows: in Section 2, we discuss the theory of polarized radiative transfer in curved spacetime, as well as different methods for solving the governing equations. We also present `RAPTOR`'s representation of polarized radiation. In Section 3, we construct a numerical algorithm that solves the polarized radiative-transfer equation and analyze that equation's stiffness with respect to our integrator, using the results to optimize our algorithm's accuracy. We demonstrate the correctness of our algorithm by comparing `RAPTOR` output to previous results, as well as the output of other codes, in the context of complex, astrophysical problems in Section 4. We summarize our results in Section 5.

2. Polarized Radiative Transfer In Curved Spacetime

Electromagnetic radiation is the most ubiquitous messenger of information in astrophysics. Emitted by sources widely distributed in space and time, it pervades the universe and interacts with matter, most of which exists as a plasma. Some of this radiation is emitted in a highly polarized state, such as synchrotron radiation. Some of it is (de)polarized after emission, for example, by interaction with magnetized plasmas (Aitken et al. 2000) or dust grains (Davis and Greenstein 1951). Besides interaction with matter, propagation of polarized radiation through curved spacetime can also affect the radiation's polarization state (Misner et al. 1973).

In Bronzwaer et al. (2018), we represented an 'unpolarized' ray of light by its intensity I_ν (where ν is the radiation frequency), position x^μ, and wave vector k^μ, the wave vector describing the ray's traveling direction and frequency, in order to solve the radiative-transfer equation along null geodesics. In the case of polarized radiative transfer, one must additionally keep track of the ray's polarization state, which describes the orientation and phase of the electromagnetic oscillations associated with the ray. In the case of an ensemble of photons with identical polarization states, the polarization state is said to be pure, while in the case of an ensemble of photons with different polarization states, the polarization state is mixed. As before, `RAPTOR` functions in the regime of geometrical optics, in which the radiation's wavelength must be much smaller than the typical length scales of plasma features and spacetime curvature.

2.1. Descriptions of a polarized ray; propagation through a curved spacetime

Various descriptions of the polarization state of radiation are used in the literature. These descriptions differ in three key ways: *i*) whether or not they encode the phase of the polarization state; *ii*) whether or not they can describe mixed states or only pure states; and *iii*) whether or not they are Lorentz covariant.

Note that in the present context, we neglect all information about the phase of the polarization state. This is because ray tracing is valid only in the regime of geometrical optics, in which the phase is omitted, so that wave effects (such as interference and diffraction) are neglected. We do, however, choose to incorporate a description of mixed states, as astrophysical sources can emit polarized radiation in such states. Additionally, a particular description may be more suitable than others, depending on the circumstances. For example, interaction with a radiating plasma is commonly described using the Stokes parameters, while the effects of propagation through curved spacetime are more easily calculated using a Lorentz-covariant description. It is therefore necessary to be able to convert between the different descriptions. In this section we describe the two descriptions of a polarized ray used in `RAPTOR`, as well as the transformation equations between them. We then present the equations of motion through curved spacetime for a polarized ray.

2.1.1. Stokes parameters

The Stokes parameters, denoted I, Q, U, V, describe a ray's polarization state by encoding the total intensity of radiation, the intensities of the two types of linear polarization, and the circularly polarized intensity, respectively. The Stokes parameters must be defined in a particular coordinate system such that the wave vector of the associated radiation is parallel to the coordinate system's z-axis. Their signs are then determined by choosing a convention, i.e., a handedness and orientation of the observer coordinate frame. This paper follows the IAU/IEEE convention, in which the angle $\chi = 1/2 \arctan(U/Q)$, called the electric vector position angle (EVPA), is defined as an angle East of North, and the sense of circular polarization is called right-handed (left handed) if the direction of rotation of the EVPA is clockwise (anti-clockwise) for an observer looking in the direction of propagation. For a detailed description of this convention, see, for example, Hamaker and Bregman (1996).

The Stokes parameters are often represented as a vector, the Stokes vector, denoted $\mathbf{S} = (I, Q, U, V)^{\mathrm{T}}$. They may also be written in terms of specific intensities, which is convenient for our purpose: $\mathbf{S}_\nu = (I_\nu, Q_\nu, U_\nu, V_\nu)^{\mathrm{T}}$. The Stokes parameters represent quantities that can be readily measured, hence they are generally used to report observational results.

The Stokes parameters can encode both pure and mixed polarization states; one can distinguish between the two using the degree of polarization, p, which is calculated as follows:

$$p = \frac{I_{\nu,\mathrm{pol}}}{I_\nu} = \frac{\sqrt{Q_\nu^2 + U_\nu^2 + V_\nu^2}}{I_\nu}, \tag{1}$$

where $I_{\nu,\mathrm{pol}}$ is the intensity of polarized radiation (which is in a pure state, described by Q_ν, U_ν, V_ν) and I_ν the total intensity. For pure polarization states, this results in $p = 1$ and $I_{\nu,\mathrm{pol}} = I_\nu$; for mixed states, we have $0 \leq p < 1$ and $I_{\nu,\mathrm{pol}} \leq I_\nu$. The Stokes parameters omit phase information, and the Stokes vector is not Lorentz covariant. Consequently, in order to transport the Stokes parameters through curved spacetime consistently, it is necessary to transport a basis vector along the geodesic, even in the case of propagation through a vacuum. Shcherbakov and Huang (2011) present an algorithm that integrates the Stokes parameters directly through curved spacetime in this manner.

Just as the Lorentz-invariant quantity $\mathcal{I} = I_\nu/\nu^3$ was employed during integration of the radiative-transfer equation in Bronzwaer et al. (2018), Lorentz-invariant Stokes intensities are defined as follows:

$$\boldsymbol{\mathcal{S}} := \frac{\mathbf{S}_\nu}{\nu^3}, \tag{2}$$

where ν represents the ray's frequency in the frame in which $\mathbf{S}_\nu$ is evaluated. It is convenient to use these Lorentz-invariant quantities during integration, when constantly shifting between frames.

2.1.2. Polarization four-vector

The polarization four-vector, f^μ, is a complex-valued vector that describes a pure polarization state. As it is a four-vector, it is Lorentz covariant. The polarization four-vector is a unit vector:

$$f^\mu f^*_\mu = 1, \tag{3}$$

where the asterisk denotes complex conjugation. The polarization vector associated with a ray is parallel-transported along the ray's null geodesic:

$$k^\alpha \nabla_\alpha f^\mu = 0. \tag{4}$$

When expressed in a suitable tetrad frame (see Section 2.2), and provided the frame is inertial, meaning that its acceleration vector vanishes, the polarization vector's components represent normalized, projected electric-field amplitudes along the frame's x and y-axes, respectively. Using Roman indices framed by parentheses to indicate tetrad-frame coordinates, we have:

$$f^{(a)} = e^{(a)}_\mu f^\mu = \begin{pmatrix} 0 \\ \hat{E}_x \\ \hat{E}_y \\ 0 \end{pmatrix}, \tag{5}$$

where $e^{(a)}_\mu$ are the components of the a-th tetrad-basis vector expressed in coordinates μ, and $\hat{E}_x$ and $\hat{E}_y$ are components of a unit vector pointing along the electric field. In the most general case, both $\hat{E}_x$ and $\hat{E}_y$ are complex, and the polarization vector encodes the polarization state's overall phase. It is also possible to restrict one of the components to be real; only the overall phase information is then lost.

The polarization four-vector only describes pure polarization states; it cannot describe mixed states. However, by keeping track of both the intensity of polarized radiation, $\mathcal{I}_{\mathrm{pol}}$ and the total intensity $\mathcal{I}$ in addition to f^μ, it is possible to represent rays with a mixed polarization state.

Given the triplet $\left(\mathcal{I}, \mathcal{I}_{\mathrm{pol}}, f^\mu\right)$, plus a suitable tetrad in which to express the Stokes parameters, the transformation $\left(\mathcal{I}, \mathcal{I}_{\mathrm{pol}}, f^{(a)}\right) \rightarrow \boldsymbol{\mathcal{S}}$ is given by

$$\boldsymbol{\mathcal{S}} = \begin{pmatrix} \mathcal{I} \\ \mathcal{Q} \\ \mathcal{U} \\ \mathcal{V} \end{pmatrix} = \begin{pmatrix} \mathcal{I} \\ \mathcal{I}_{\mathrm{pol}} \left(f^{(1)} f^{(1)*} - f^{(2)} f^{(2)*} \right) \\ \mathcal{I}_{\mathrm{pol}} \left(f^{(1)} f^{(2)*} + f^{(2)} f^{(1)*} \right) \\ i\mathcal{I}_{\mathrm{pol}} \left(f^{(1)} f^{(2)*} - f^{(2)} f^{(1)*} \right) \end{pmatrix}. \tag{6}$$

The reverse transformation, $\boldsymbol{\mathcal{S}} \rightarrow \left(\mathcal{I}, \mathcal{I}_{\mathrm{pol}}, f^{(a)}\right)$, is degenerate, as the latter quantity contains an additional degree of freedom (the overall phase of the ray's polarization state). The degeneracy is lifted by choosing a phase, i.e., by demanding that $f^{(1)} \in \mathbb{R}$. $f^{(a)}$ is then computed as follows:

$$\mathcal{I}_{\mathrm{pol}} = \sqrt{\mathcal{Q}^2 + \mathcal{U}^2 + \mathcal{V}^2}, \tag{7a}$$

$$f^{(1)} = \sqrt{\frac{1 + \tilde{Q}}{2}}, \tag{7b}$$

$$f^{(2)} = \begin{cases} 1 & \text{if } f^{(1)} = 0, \\ \dfrac{\tilde{U} - i\tilde{V}}{2f^{(1)}} & \text{otherwise,} \end{cases} \tag{7c}$$

where $\tilde{Q} \equiv \mathcal{Q}/\mathcal{I}_{\mathrm{pol}}$, and similarly for $\tilde{U}$ and $\tilde{V}$ (note that $\mathcal{I}$ retains its identity when transforming).

2.1.3. Spacetime propagation equation

In our model, the polarization state of a ray is affected by two processes: propagation through spacetime and interaction with a plasma. Given Eqs. 1 and 4, we can express the equations of motion for propagation of a polarized ray through curved (vacuum)

spacetime:

$$\left.\frac{\mathrm{d}}{\mathrm{d}\lambda}\right|_S f^\mu = -\Gamma^\mu_{\alpha\rho} k^\alpha f^\rho, \tag{8a}$$

$$\left.\frac{\mathrm{d}}{\mathrm{d}\lambda}\right|_S \mathcal{I} = 0, \tag{8b}$$

$$\left.\frac{\mathrm{d}}{\mathrm{d}\lambda}\right|_S \mathcal{I}_{\mathrm{pol}} = 0, \tag{8c}$$

where λ is the affine parameter, expressed in units of length (GM/c^2), which parametrizes the null geodesic. The subscript S implies that we only consider effects due to propagation through curved spacetime, ignoring the plasma. Equations 8a-8c show that the degree of polarization p remains constant along a ray when propagated through a curved (vacuum) spacetime. This is a consequence of the fact that $I_{\nu,\mathrm{pol}}$ and I_ν transform in the same way between different frames, so that their ratio remains a constant from frame to frame, and thus throughout a (vacuum) spacetime integration. Equivalently, the corresponding Lorentz-invariant intensities $\mathcal{I}$ and $\mathcal{I}_{\mathrm{pol}}$ are themselves constant along the ray, as is the ratio between them.

2.2. Constructing suitable tetrad frames in which to express the Stokes parameters

As in the case of unpolarized radiative transfer, it will be convenient to perform the radiative-transfer computations in a suitably chosen frame. Unlike in the case of unpolarized radiative transfer (where transforming between frames is accomplished simply by computing a ray's frequency seen by an observer co-moving with the frame of interest), this frame must now be constructed explicitly, as polarized radiative-transfer computations depend on the orientation of the frame. This must be done both at the observer's location (the camera) and also at any location where the ray interacts with radiating matter. It is also necessary to specify the handedness of the tetrad frame, which is achieved by ordering its basis vectors.

We employ a generalized version of the tetrad described in Gammie and Leung (2012); as is the case for those authors, our tetrad-frame indices $(t, \|, \perp, K)$ correspond with (t, x, y, z), respectively, defining a right-handed coordinate system. As previously, we adopt the $(-,+,+,+)$ metric convention, and we denote the tetrad-frame coordinates with Roman indices enclosed in parentheses. In what follows, it is assumed that the ray's wave vector is null ($k_\alpha k^\alpha = 0$), that the frame's velocity four-vector is timelike with norm -1, i.e., $u_\alpha u^\alpha = -1$, and that d^α is a spacelike vector ($d_\alpha d^\alpha > 0$). When the ray resides inside the volume for which GRMHD data is available, u^α is given by the local plasma four-velocity, and we may use the local magnetic-field four vector (b^α) for the spacelike vector d^α; b^α is spacelike (except for the pathological case in which it vanishes, in which case the integration step may be skipped), and orienting the tetrad this way will simplify calculations because all coefficients related to Stokes U vanish. Under these circumstances we shall refer to the tetrad frame as the plasma frame. When no magnetic-field vector is available, or when we wish to orient the tetrad in a specific way (e.g., in order to represent a particular observer's position and attitude), the trial vector d^α must be constructed in such a way that it is spacelike. This generally happens at the observer's location, in which case we shall refer to the tetrad as the observer frame; the velocity four-vector in such cases is generally chosen to be stationary, so that $u_{\mu,\mathrm{obs}} = (u_t, 0, 0, 0)$. Since u^t is a constant, the observer frame is an inertial frame. Note that the tetrad must be constructed so as to respect the IAU/IEEE observer convention (Hamaker and Bregman 1996).

To construct a tetrad frame for a ray, we start by defining the intermediate quantities

$$d^2 \coloneqq d_\alpha d^\alpha, \tag{9a}$$

$$\beta \coloneqq u_\alpha d^\alpha, \tag{9b}$$

$$\omega \coloneqq -k_\alpha u^\alpha, \tag{9c}$$

$$C \coloneqq \frac{k_\alpha d^\alpha}{g} - \beta, \tag{9d}$$

$$\mathcal{N} \coloneqq \sqrt{d^2 + \beta^2 - C^2}. \tag{9e}$$

The tetrad is then constructed as follows, using the Gram-Schmidt orthonormalization procedure:

$$e^\mu_{(t)} = u^\mu\,, \tag{10a}$$

$$e^\mu_{(K)} = \frac{k^\mu}{\omega} - u^\mu\,, \tag{10b}$$

$$e^\mu_{(\|)} = \frac{d^\mu + \beta u^\mu - C e^\mu_{(K)}}{\mathcal{N}}\,, \tag{10c}$$

$$e^\mu_{(\perp)} = \frac{\epsilon^{\mu\nu\alpha\beta} u_\nu k_\alpha d_\beta}{\omega\mathcal{N}}\,, \tag{10d}$$

where

$$\epsilon^{\mu\nu\alpha\beta} = -\frac{1}{\sqrt{-g}}\,[\mu\nu\alpha\beta]\,, \tag{11}$$

is the Levi-Civita tensor, $[\mu\nu\alpha\beta]$ is the permutation symbol, and $g \equiv \det\left(g_{\mu\nu}\right)$. Note that the general metric tensor $g_{\mu\nu}$ acts on coordinate-frame indices while the Minkowski metric tensor $\eta_{\mu\nu}$ acts on fluid-frame indices, e.g., $g_{\mu\nu} \to \eta_{\mu\nu}$ in the fluid frame.

2.3. Plasma interaction; synchrotron emission, absorption, and Faraday rotation coefficients

The ray's interaction with a plasma is most conveniently expressed using the Stokes parameters. Given the plasma frame, we require a set of emission, absorption, and rotation coefficients j, α, and ρ, respectively. The coefficients used in `RAPTOR` are adapted from Dexter (2016). They are recapitulated in Appendix C. Note that the coefficients must be expressed in their Lorentz-invariant form (Section 2.1.1). The effect of the plasma on the invariant Stokes parameters is given by

$$\left.\frac{\mathrm{d}}{\mathrm{d}\lambda}\right|_P \begin{pmatrix}\mathcal{I}\\ \mathcal{Q}\\ \mathcal{U}\\ \mathcal{V}\end{pmatrix} = \begin{pmatrix} j_I\\ j_Q\\ j_U\\ j_V\end{pmatrix} - \begin{pmatrix} \alpha_I & \alpha_Q & \alpha_U & \alpha_V\\ \alpha_Q & \alpha_I & \rho_V & -\rho_U\\ \alpha_U & -\rho_V & \alpha_I & \rho_Q\\ \alpha_V & \rho_U & -\rho_Q & \alpha_I\end{pmatrix}\begin{pmatrix}\mathcal{I}\\ \mathcal{Q}\\ \mathcal{U}\\ \mathcal{V}\end{pmatrix}, \tag{12}$$

with the subscript P implying that only the ray's interaction with the plasma is taken into account (ignoring the effects due to spacetime propagation).

3. Implementation

In this section, we develop algorithms in order to implement the polarized radiative-transfer formalism described in Section 2 in `RAPTOR`. The main challenge in this implementation lies in the fact that the polarized radiative-transfer equation, Eq. 12, may become stiff with respect to explicit integrators depending on the plasma conditions. To mitigate this problem, we analyze when

stiffness occurs, and develop an implicit integrator for such integration steps. Precise knowledge of where stiffness occurs is crucial when it comes to minimizing the number of implicit steps, which are less accurate, although much more stable.

3.1. Integration strategy

As in the case of unpolarized radiative transfer through curved spacetime, the integration can be thought of as consisting of two parts: vacuum integration (which takes care of the effects on a ray's polarization state due purely to traveling through curved spacetime) and plasma integration (which describes the ray's interaction with the plasma through the plasma's emission, absorption, and rotation coefficients (Section 2.3)). The two subproblems are handled with separate routines. During an integration step, and when the ray resides in a radiating plasma, the plasma interaction is computed first, after which a spacetime-propagation step is taken (as if through a vacuum). When the ray resides in vacuum, the plasma-integration step is omitted.

3.2. Numerical scheme for plasma integration

In order to take a ray's interaction with the radiating plasma into account, we must solve Eq. 12 numerically. Note that, due to aligning the frame so that the Stokes U polarization mode is parallel to the plasma's magnetic-field vector, we have $j_U = \alpha_U = \rho_U = 0$. Depending on the local values of the emission, absorption, and rotation coefficients, Eq. 12 may be a stiff equation for explicit integration schemes. Note that the condition for stiffness is different for each explicit integrator, and that it does not directly depend on any particular physical quantity, but rather on the product of the local step size taken by `RAPTOR` and the largest eigenvalue of the matrix appearing in Eq. 12 (see, e.g., Gautschi (2011)). `RAPTOR` uses the fourth-order Runge-Kutta (RK4) explicit integrator (see below); an analysis of when Eq. 12 becomes stiff for the explicit RK4 integrator is presented in Appendix A. The result of that analysis is a numerical stiffness check that is performed at each integration step.

Stiff equations are practically impossible to solve using forward integration methods of the order considered so far in `RAPTOR`; the solution will become unstable, and prohibitively small step sizes are required. Implicit integration methods are much more stable, and can be applied even to stiff problems. However, they tend to dampen rapid oscillations, which increases the stability, but which comes at the cost of less accuracy. In order to integrate Eq. 12, Dexter (2016) employs three integration strategies: an implicit-explicit integrator routine from the `LSODA` package, an implementation of the DELO method (Rees et al. 1989), and an explicit quadrature method based on the work of Landi Degl'Innocenti and Landi Degl'Innocenti (1985). Mościbrodzka et al. (2016) employs a semi-analytical solution also based on Landi Degl'Innocenti and Landi Degl'Innocenti (1985), as well as a three-step numerical integration routine. We choose to develop a novel implicit-explicit integrator for `RAPTOR`. Since stiffness conditions vary throughout the plasma, using only implicit methods may needlessly sacrifice accuracy in regions where Eq. 12 is not stiff. Switching to an explicit integration scheme in such regions improves the overall accuracy of the computation.

For explicit integration steps, our algorithm uses the RK4 integrator:

$$\mathbf{C}_{1,\boldsymbol{\mathcal{S}}} = \Delta\lambda \cdot \mathbf{F}\left(\boldsymbol{\mathcal{S}}\right), \tag{13a}$$

$$\mathbf{C}_{2,\boldsymbol{\mathcal{S}}} = \Delta\lambda \cdot \mathbf{F}\left(\boldsymbol{\mathcal{S}} + \frac{1}{2}\mathbf{C}_{1,\boldsymbol{\mathcal{S}}}\right), \tag{13b}$$

$$\mathbf{C}_{3,\boldsymbol{\mathcal{S}}} = \Delta\lambda \cdot \mathbf{F}\left(\boldsymbol{\mathcal{S}} + \frac{1}{2}\mathbf{C}_{2,\boldsymbol{\mathcal{S}}}\right), \tag{13c}$$

$$\mathbf{C}_{4,\boldsymbol{\mathcal{S}}} = \Delta\lambda \cdot \mathbf{F}\left(\boldsymbol{\mathcal{S}} + \mathbf{C}_{3,\boldsymbol{\mathcal{S}}}\right), \tag{13d}$$

where $\mathbf{F}$ represents the right-hand-side of Eq. 12. A single explicit integration step proceeds as follows:

$$\boldsymbol{\mathcal{S}}_{new} = \boldsymbol{\mathcal{S}} + \frac{1}{6}\left(\mathbf{C}_{1,\boldsymbol{\mathcal{S}}} + 2\mathbf{C}_{2,\boldsymbol{\mathcal{S}}} + 2\mathbf{C}_{3,\boldsymbol{\mathcal{S}}} + \mathbf{C}_{4,\boldsymbol{\mathcal{S}}}\right). \tag{14}$$

For implicit steps, our algorithm uses the (second-order) implicit trapezoid method:

$$\boldsymbol{\mathcal{S}}_{new} = \boldsymbol{\mathcal{S}} + \frac{\Delta\lambda}{2}\left[\left(\mathbf{j} - \mathbf{M}\boldsymbol{\mathcal{S}}_{new}\right) + \left(\mathbf{j} - \mathbf{M}\boldsymbol{\mathcal{S}}\right)\right], \tag{15}$$

where $\mathbf{j} = (j_I, j_Q, j_U, j_V)^{\mathrm{T}}$ and $\mathbf{M}$ is the 4-by-4 matrix appearing in Eq. 12. Since Eq. 12 is linear, the implicit trapezoid method for this equation yields an explicit equation for $\boldsymbol{\mathcal{S}}_{new}$ using an LU-decomposition, so that there is no root-finding penalty even for implicit steps (see Appendix B).

3.3. Numerical scheme for vacuum integration

Previously we integrated a ray's position, x^α, as well as its wave vector, k^α, through arbitrary, curved spacetimes. We must now also keep track of the description of the ray's polarization state, which is captured in the polarization vector f^μ; in other words, we must solve Eq. 8a.

As before, we use a fourth-order Runge-Kutta scheme to integrate the ray backward, i.e., starting at the camera. After a stopping condition has been reached (e.g., the ray plunges into the horizon, or it reaches the outer boundary of a GRMHD simulation), polarized radiative transfer proceeds in the forward direction, i.e., toward the camera. We extend Eqs. 7-14 from Bronzwaer et al. (2018) (noting that forward integration, i.e., from the plasma toward the camera, is employed) to include the polarization vector as follows:

$$C_{1,f^\alpha} = \Delta\lambda \cdot F^\alpha\left(x^{\underline{i}}, k^{\underline{i}}, f^{\underline{i}}\right), \tag{16a}$$

$$C_{2,f^\alpha} = \Delta\lambda \cdot F^\alpha\left(x^{\underline{i}} + \tfrac{1}{2}C_{1,x^{\underline{i}}}, k^{\underline{i}} + \tfrac{1}{2}C_{1,k^{\underline{i}}}, f^{\underline{i}} + \tfrac{1}{2}C_{1,f^{\underline{i}}}\right), \tag{16b}$$

$$C_{3,f^\alpha} = \Delta\lambda \cdot F^\alpha\left(x^{\underline{i}} + \tfrac{1}{2}C_{2,x^{\underline{i}}}, k^{\underline{i}} + \tfrac{1}{2}C_{2,k^{\underline{i}}}, f^{\underline{i}} + \tfrac{1}{2}C_{2,f^{\underline{i}}}\right), \tag{16c}$$

$$C_{4,f^\alpha} = \Delta\lambda \cdot F^\alpha\left(x^{\underline{i}} + C_{3,x^{\underline{i}}}, k^{\underline{i}} + C_{3,k^{\underline{i}}}, f^{\underline{i}} + C_{3,f^{\underline{i}}}\right), \tag{16d}$$

where, as in Bronzwaer et al. (2018), underlined indices are a notational shorthand to indicate that all coordinate indices occur in the right-hand side of these equations, and F^α represents the right-hand side of Eq. 8a. Given these coefficients, an integration step proceeds as follows:

$$f^\alpha_{new} = f^\alpha + \frac{1}{6}\left(C_{1,f^\alpha} + 2C_{2,f^\alpha} + 2C_{3,f^\alpha} + C_{4,f^\alpha}\right). \tag{17}$$

4. Code Verification

In this section we aim to verify the correctness of RAPTOR output by comparing it to analytical results as well as output from different codes. For this purpose, a number of verification tests were selected from the literature and reproduced using RAPTOR. Convergence tests were also performed for all integrators described in the previous section.

4.1. Plasma-integration test; comparison to analytical solution

As a first step, we test our numerical integrator for Eq. 12, i.e., the ray's interaction with the radiating plasma. Note that the two tests reproduced in this section were also reproduced by Dexter (2016) and Moscibrodzka and Gammie (2017), the latter of which performed the test using non-standard 'snake' coordinates, which means that the space-time integration routine is tested simultaneously in their case, making it a more challenging test. In each case, the initial conditions are $I = Q = U = V = 0$ and the stepsize is $\Delta s = 0.003$.

In the first plasma test, $j_I = 2$, $j_Q = 1$, $\alpha_I = 1$, and $\alpha_Q = 1.2$ (all other coefficients vanish). Figure 1 shows the integration results for this test using the RK4 algorithm, while Fig. 2 shows the results for the implicit trapezoid algorithm. In the second plasma test, $j_Q = j_U = j_V = 0.1$, $\rho_Q = 10$, and $\rho_V = -4$ (again, all other coefficients vanish). Figure 3 shows the integration results for this test using the RK4 algorithm, while Fig. 4 shows the results for the implicit trapezoid algorithm. Note the difference in scale of the errors for the implicit trapezoid scheme versus the explicit RK4 scheme - the RK4 scheme, being of a higher order, produces a more accurate result in both cases. On the other hand, the implicit trapezoid scheme is much more robust with respect to increasing the step size, as is shown in Fig. 5, which is a repeat of Fig. 4, but with a stepsize that is 100 times larger than previously. Using these settings, the RK4 scheme fails to produce a meaningful result, and the error diverges; the trapezoid scheme, on the other hand, remains stable, although the accuracy is affected by the large stepsize.

Error-convergence plots for both routines are shown in Figs. 6 and 7 (to compute the error for these plots, the absolute difference between the exact and the numerical solution was taken at the end of integration, where $\lambda = 3$.)

4.2. Spacetime-integration test; thin-disk model

Next, we test our integrator for Eq. 8a, i.e., the equation for propagation of a polarized ray through spacetime. We do so in a spacetime devoid of matter, save for a geometrically thin, optically thick accretion disk in the equatorial plane, based on the description by Shakura and Sunyaev (1973) and Novikov and Thorne (1973). The blackbody radiation emitted by the disk is scattered by electrons in the disk's atmosphere. The radiation is limb-darkened by the disk's atmosphere (note that the atmosphere is not represented in the geometry of the model, but its effects are taken into account by modifying the emission coefficient), and it is partially linearly polarized in the plane of the disk, perpendicular to both the wave vector and the disk normal, as in the model presented in Chandrasekhar (1960) and studied in Connors et al. (1980) and Schnittman and Krolik (2009). In this model, the emission coefficients are delta functions along the ray; they are evaluated once, after which the polarized light is transported through the vacuum, allowing us to test the vacuum-

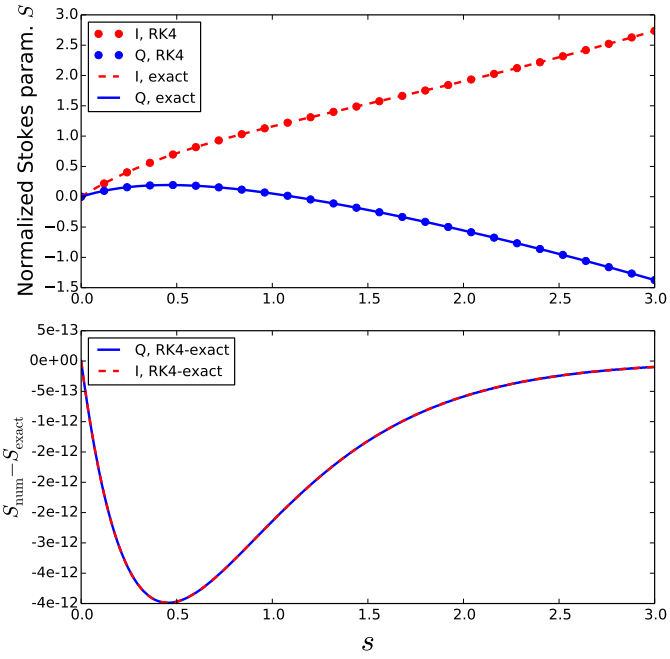

Fig. 1: A plot of Stokes I and Q (in normalized units) as a function of distance traveled s, using the explicit Runge-Kutta integration routine, for the first flat-spacetime plasma-integration test.

integration routine (this result was earlier reproduced in Dexter (2016)).

Figure 8 shows the results obtained using the settings specified by an EHT internal note on polarized radiative transfer;

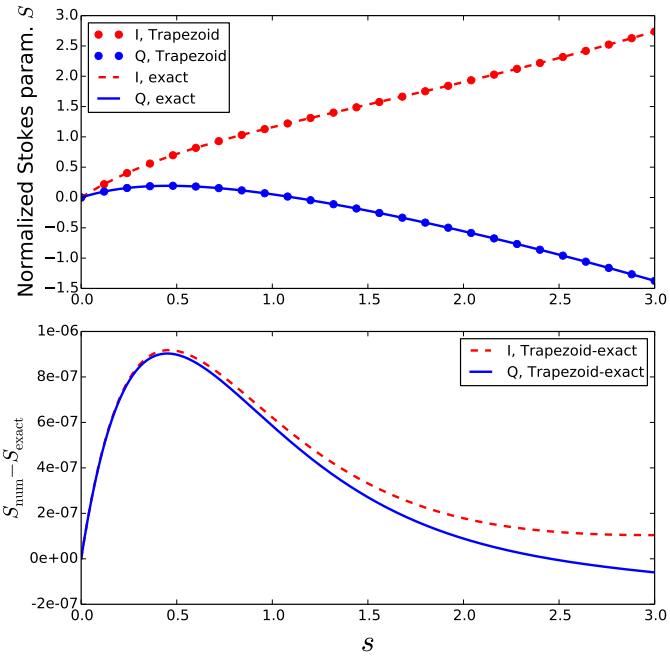

Fig. 2: A plot of Stokes I and Q (in normalized units) as a function of distance traveled s, using the implicit trapezoid integration routine, for the first flat-spacetime plasma-integration test.

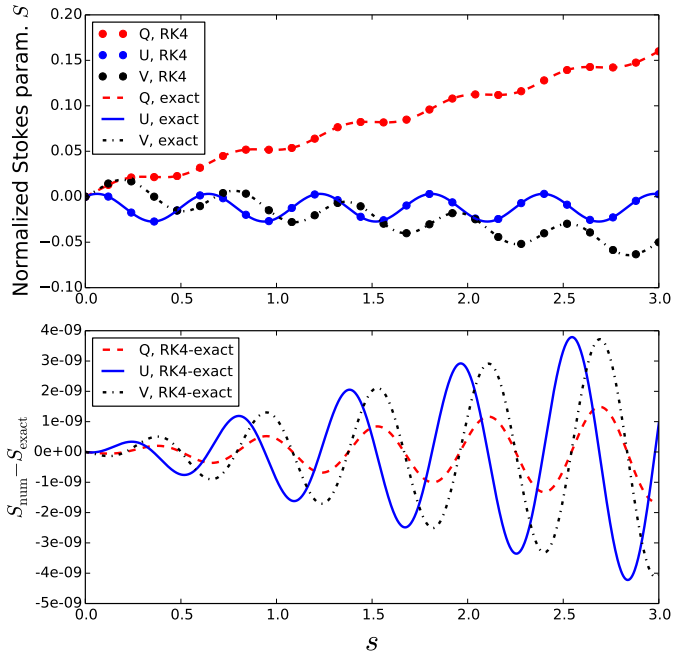

Fig. 3: A plot of Stokes Q, U, and V (in normalized units) as a function of distance traveled s, using the RK4 integration routine, for the second flat-spacetime plasma-integration test.

these settings are listed in Table 2. The integrated flux densities for all Stokes parameters are reported in Table 1. Note that, although we report the results in units of Jansky per pixel for continuity with the rest of the paper, the camera frequency for

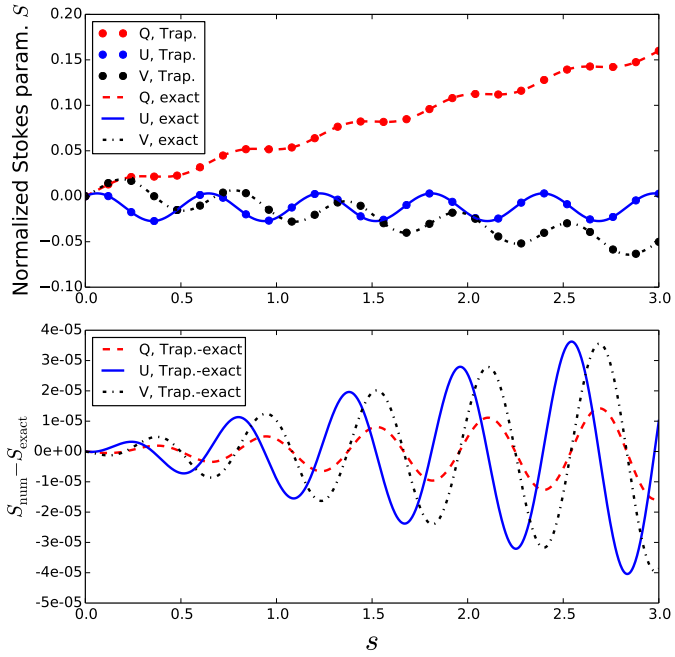

Fig. 4: A plot of Stokes Q, U, and V (in normalized units) as a function of distance traveled s, using the implicit trapezoid integration routine, for the second flat-spacetime plasma-integration test.

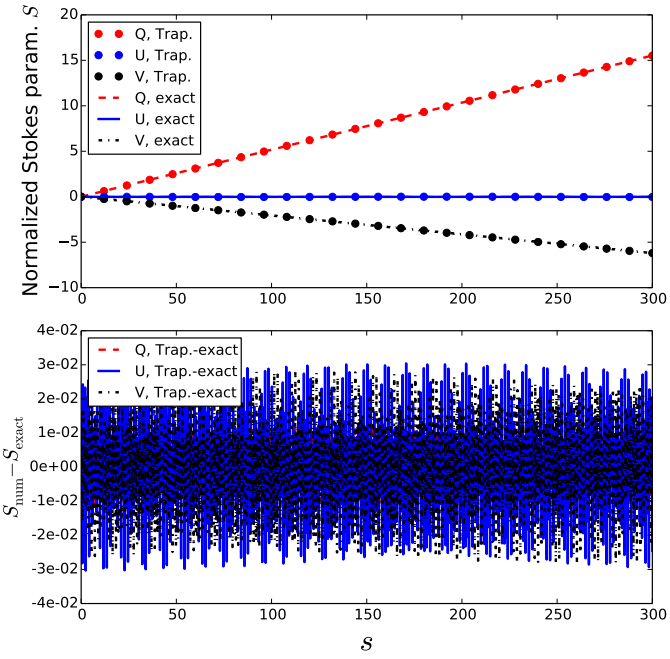

Fig. 5: As Fig. 4, but with a stepsize that is 100 times bigger, so the range of s is 100 times larger as well. Note that the implicit trapezoid algorithm remains stable; the RK4 algorithm breaks down (the error diverges) under these conditions.

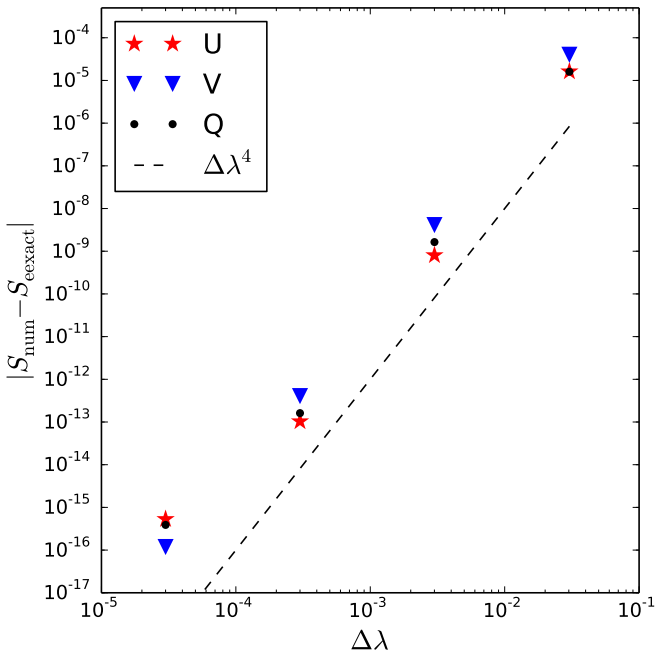

Fig. 6: Stepsize-convergence plot for the 4th-order Runge-Kutta (RK4) plasma-integration routine, for the second plasma test (see Section 4.1). The error is proportional to $\Delta\lambda^4$, as is expected. The fact that the leftmost datapoint is slightly offset from the convergence line suggests that the machine precision, which is of order 1e−16 for the double-precision arithmetic used in `RAPTOR`, is reached.

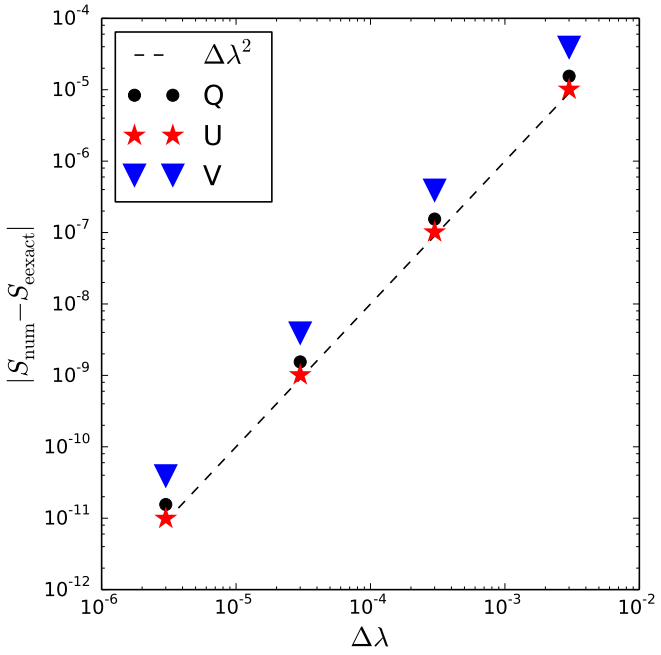

Fig. 7: Stepsize-convergence plot for the implicit trapezoid (IT) plasma-integration routine, for the second plasma test (see Section 4.1). The error is proportional to $\Delta\lambda^2$, as is expected.

this result was in the X-ray part of the electromagnetic spectrum. Figure 9 shows the same result but, in the 'polarization vector representation', to be compared with Fig. 1 in Schnittman and Krolik (2009). Figure 9 also uses a value of 0.9 for the black-hole spin, as did those authors.

Flux	Thin disk	GRMHD low	GRMHD high
$S_{\nu,I}$ (Jy)	$6.869 \cdot 10^6$	0.0102	0.494
$S_{\nu,Q}$ (Jy)	$-1.586 \cdot 10^5$	−0.000312	−0.00722
$S_{\nu,U}$ (Jy)	$1.057 \cdot 10^4$	0.00032	−0.00328
$S_{\nu,V}$ (Jy)	0	$-6.96 \cdot 10^{-6}$	0.00333

Table 1: Integrated flux densities for all Stokes parameters for the thin-disk test (Section 4.2) as well as the low- and high-flux versions of the GRMHD test (Section 4.1). Images of these tests (albeit at a modified field of view and camera resolution) are shown in Figs. 8, 11, and 12.

Figure 10 shows the stepsize-convergence plot for the RK4 spacetime-integration routine (which integrates Eq. 8a). The error was computed by tracking the norm of the polarization vector, which should be conserved after integration of the ray, which passes close to the black hole, through a strongly curved region of spacetime.

4.3. Spacetime-and-plasma (GRMHD) integration test

Finally, we test the combination of the vacuum and plasma-integration routines. To do so, the rays must propagate through a radiating plasma that is of finite extent (i.e., not infinitesimally thin), so that plasma interaction takes place as the rays are propagating through curved spacetime. This may be achieved using data from a GRMHD simulation of an accreting AGN; a particular data dump, created using the `HARM` code (Gammie et al. 2003), was used for these tests, which are part of the EHT's internal code-comparison efforts for polarized radiative transfer, a forthcoming publication. The radiative model uses the thermal-synchrotron emission, absorption, and rotation coefficients listed in C, uses a constant proton-to-electron temperature ratio of 3, making for a disk-dominated emission model. To reproduce the results listed in this paper, please refer to Table 2, which shows the `RAPTOR` settings used to generate the test results for two scenarios (the low-accretion-rate and high-accretion-rate scenarios, respectively); the GRMHD dump that was used to generate these results is distributed along with `RAPTOR`. The resulting images (Figs. 11 and 12) show a low-luminosity AGN at a low inclination angle (163 degrees, or 17 degrees from the southern pole). A radial pattern is observed. Table 1 lists the flux densities obtained for the thin-disk and GRMHD tests.

Parameter	Thin-disk test value	GRMHD test value
a	0.99	0.94
$M_{\rm BH}$	$10M_\odot$	$6.2 \cdot 10^9 M_\odot$
$d_{\rm source}$	0.05 pc	16.9 Mpc
ν_{cam}	$2.417989 \cdot 10^{17}$ Hz	230 GHz
r_{cam}	$10^4 R_G$	$10^4 R_G$
θ_{cam}	75 deg	163 deg
ϕ_{cam}	0	0
$DX = DY$	$40\ R_G$	$44.17 R_G$
$NX = NY$	80 px	160 px
$\dot{M}$	$1.399 \cdot 10^{17}$g/s	–
$\mathcal{M}_{\rm low}$	–	$1.672 \cdot 10^{26}$ g
$\mathcal{M}_{\rm high}$	–	$2.739 \cdot 10^{25}$ g

Table 2: Settings used to reproduce the thin-disk test (Section 4.2) as well as the low- and high-flux versions of the GRMHD test (Section 4.1). The test results are recapitulated in Table 1.

4.4. Convergence with other polarized radiative-transfer codes

The thin-disk and GRMHD tests discussed in the previous two sections have been adopted by the EHT's collaborative effort to establish convergence between polarized general-relativistic radiative transfer codes, which is to be published in a forthcoming paper. At the time of publication, comparison to `ipole` output for the same tests yielded an agreement to order 1% in terms of mean squared error. Experience has revealed a few possible sources of error, such as the precise camera setup used, or the approximations used to compute Bessel functions in the emission/absorption/rotation coefficients. However, since there are uncertainties that are larger than 1% in such aspects of the computation as the microphysics (e.g., the energy-distribution functions of the radiating electrons, which is affected by magnetic reconnection, fine-scale turbulence and shockwaves, etc.), the agreement that has been achieved is sufficient for current EHT science goals. Nevertheless, these results may be refined further, and are to be published in a forthcoming EHT paper comparing methods for polarized general-relativistic radiative transfer.

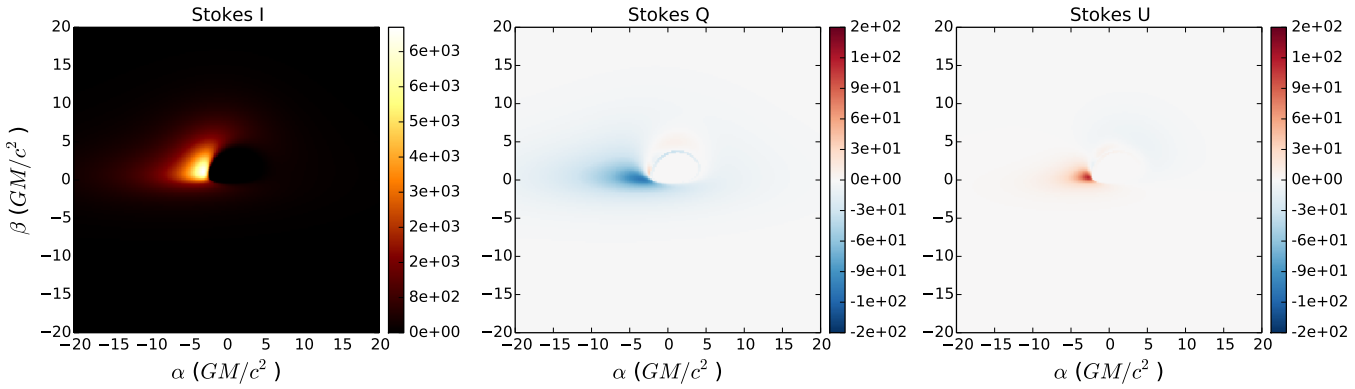

Fig. 8: Polarized image of the thin-disk model from Schnittman and Krolik (2009) in terms of the Stokes parameters. The image size is 200 by 200 pixels. Flux is given in Jy px^{-1} (Jansky per pixel). Stokes V is omitted, as it vanishes due to the symmetry of the problem.

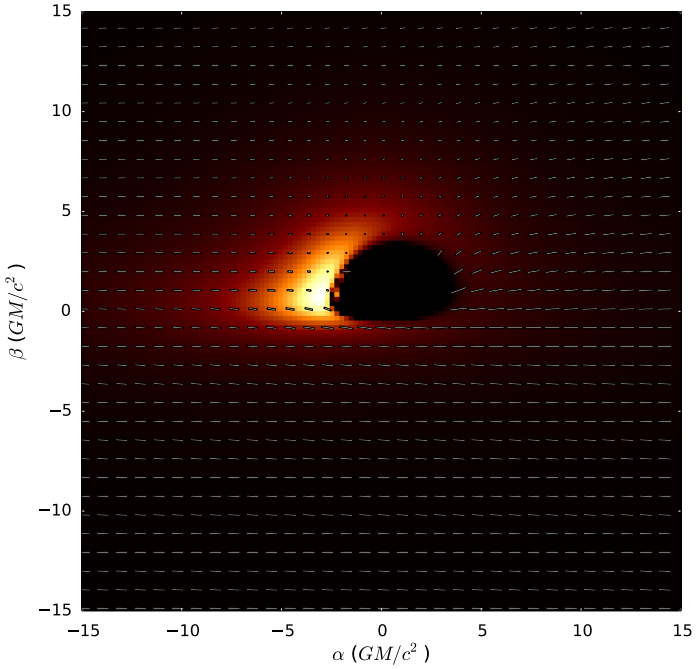

Fig. 9: Polarized image of the thin-disk model from Schnittman and Krolik (2009) shown with polarization vectors.

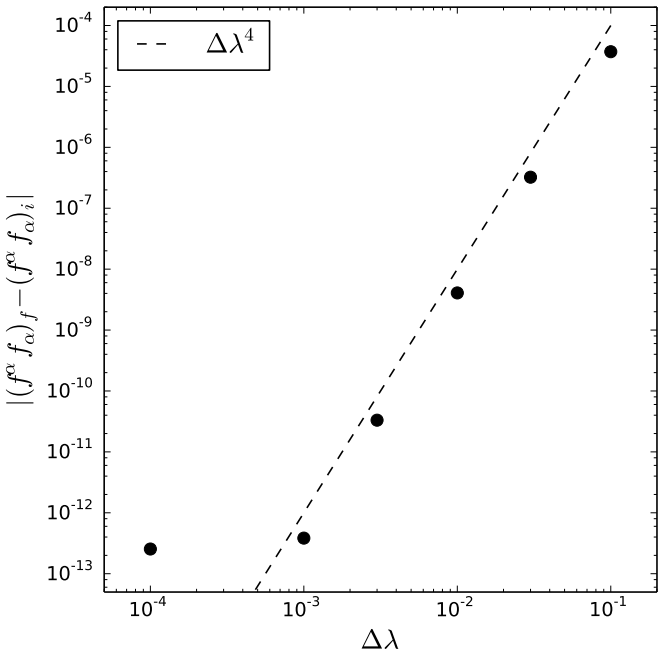

Fig. 10: Stepsize-convergence plot for the 4th-order Runge-Kutta (RK4) spacetime-transport routine, for a particular ray in the thin-disk test (see Section 4.2). The error is proportional to $\Delta\lambda^4$, as is expected.

5. Summary

In order to deepen understanding of polarized observations of astrophysical phenomena originating in strong gravitational fields, we have developed a code capable of performing efficient polarized radiative transfer in arbitrary spacetimes. Our implementation can represent a polarized ray using both the Stokes vector and the polarization vector (plus relevant intensities), and can switch between the two. The former description is appropriate for plasma interactions (whenever the ray is inside a plasma), while the latter presents a better description for spacetime propagation. This formalism is conceptually simple and uses the minimum number of degrees of freedom.

The polarized radiative-transfer equation, which describes a ray's interaction with a plasma, may become stiff in some regions of the integration volume, while being much easier to integrate in others. We have developed a computationally efficient yet robust implicit-explicit scheme to integrate this equation. In order to maximize accuracy and efficiency, our algorithm switches between implicit and explicit integration schemes. We have determined when the polarized radiative-transfer equation (as expressed in our particular tetrad frame) becomes stiff for the fourth-order Runge-Kutta integrator in order to establish the switching criterium.

We have demonstrated correctness of our new algorithms for spacetime propagation and plasma interaction separately as well as together. Comparison of `RAPTOR` output for the thin-disk and GRMHD tests described in Sections 4.2 and 4.3 to that of `ipole` show excellent agreement, strongly suggesting that the two different implementations agree on the physics to a sufficient de-

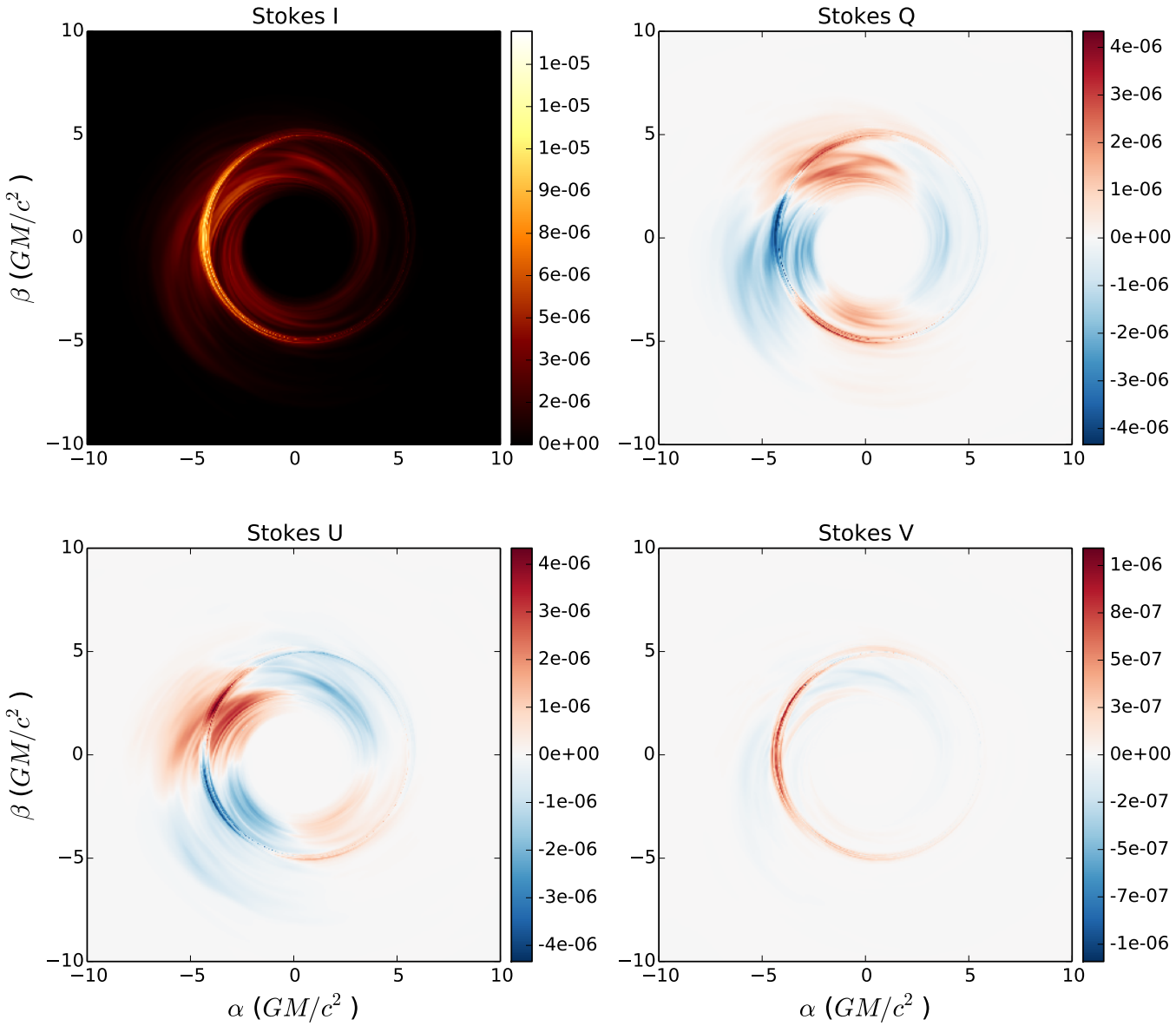

Fig. 11: Polarized image of the GRMHD-based third test for the high-accretion-rate scenario. In order to enhance the clarity of these images, we have chosen a different field of view from the original test (see Table 2); the camera size for these images is 20 by 20 R_G, and the image size is 1024 by 1024 pixels. Flux is given in Jy px^{-1} (Jansky per pixel). The integrated flux densities, useful for code-comparison purposes, are recapitulated in Table 1.

gree of accuracy for the Event Horizon Telescope, in the context of a relevant, complex astrophysical problem. The value in that result lies both in adding credence to the EHT's theoretical calculations pertaining to polarized sources such as M87, and in providing a new, public tool for the efficient production of simulated, polarized observations.

Polarized observations have the potential to allow observers to determine the structure of magnetic fields in the accretion disks and jets of black holes. Meanwhile, theoretical investigations probe the observational effects produced by different plasma models (see, e.g., Jiménez-Rosales and Dexter 2018; Palumbo et al. 2020), and even different theories of gravity (Mizuno et al. 2018). RAPTOR can be used as an efficient and flexible tool with which to explore the radiative properties of different plasma models in arbitrary spacetimes. Such simulations are to be compared with current and future observations of polarized radiation emitted by relativistic plasma's orbiting black holes, neutron stars, and potentially other, more exotic objects.

Acknowledgements

This work is supported by the ERC Synergy Grant "BlackHoleCam: Imaging the Event Horizon of Black Holes" (Grant 610058). ZY is supported by a Leverhulme Trust Early Career Fellowship. The authors thank Koen de Boer, Monika Mościbrodzka, Ben Prather, George Wong, and the anonymous referee for their helpful suggestions regarding the manuscript. This work has made use of NASA's Astrophysics Data System (ADS).

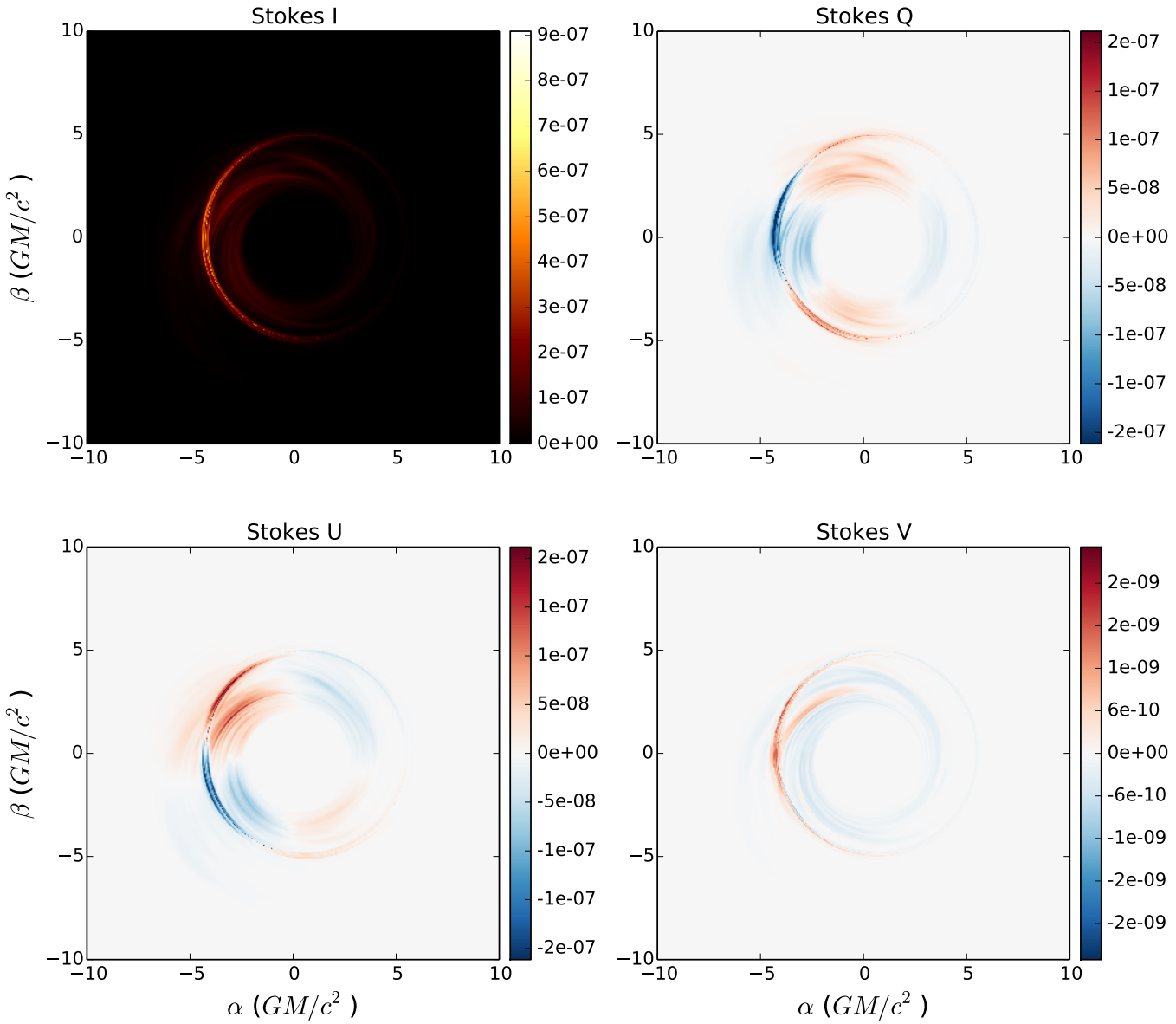

Fig. 12: Polarized image of the GRMHD-based third test for the low-accretion-rate scenario. In order to enhance the clarity of these images, we have chosen a different field of view from the original test (see Table 2); the camera size for these images is 20 by 20 R_G, and the image size is 1024 by 1024 pixels. Flux is given in Jy px^{-1} (Jansky per pixel). The integrated flux densities, useful for code-comparison purposes, are recapitulated in Table 1.

References

Aitken, D. K., Greaves, J., Chrysostomou, A., Jenness, T., Holland, W., Hough, J. H., Pierce-Price, D., and Richer, J. (2000). Detection of Polarized Millimeter and Submillimeter Emission from Sagittarius A*. *ApJ*, 534(2):L173–L176.

Bower, G. C., Wright, M. C. H., Falcke, H., and Backer, D. C. (2003). Interferometric Detection of Linear Polarization from Sagittarius A* at 230 GHz. *ApJ*, 588:331–337.

Broderick, A. and Blandford, R. (2004). Covariant magnetoionic theory - II. Radiative transfer. *MNRAS*, 349(3):994–1008.

Broderick, A. E. (2006). Radiative transfer along rays in curved space-times. *MNRAS*, 366:L10–L12.

Broderick, A. E. and Loeb, A. (2006). Imaging optically-thin hotspots near the black hole horizon of Sgr A* at radio and near-infrared wavelengths. *MNRAS*, 367(3):905–916.

Broderick, A. E. and Narayan, R. (2006). On the Nature of the Compact Dark Mass at the Galactic Center. *ApJ*, 638(1):L21–L24.

Bromley, B. C., Melia, F., and Liu, S. (2001). Polarimetric Imaging of the Massive Black Hole at the Galactic Center. *ApJ*, 555(2):L83–L86.

Bronzwaer, T., Davelaar, J., Younsi, Z., Mościbrodzka, M., Falcke, H., Kramer, M., and Rezzolla, L. (2018). RAPTOR. I. Time-dependent radiative transfer in arbitrary spacetimes. *A&A*, 613:A2.

Chandrasekhar, S. (1960). *Radiative transfer*.

Connors, P. A., Piran, T., and Stark, R. F. (1980). Polarization features of X-ray radiation emitted near black holes. *ApJ*, 235:224–244.

Davis, Leverett, J. and Greenstein, J. L. (1951). The Polarization of Starlight by Aligned Dust Grains. *ApJ*, 114:206.

Dexter, J. (2016). A public code for general relativistic, polarised radiative transfer around spinning black holes. *ArXiv e-prints*.

Dexter, J. and Agol, E. (2009). A Fast New Public Code for Computing Photon Orbits in a Kerr Spacetime. *ApJ*, 696:1616–1629.

Dexter, J., Agol, E., and Fragile, P. C. (2009). Millimeter Flares and VLBI Visibilities from Relativistic Simulations of Magnetized Accretion Onto the Galactic Center Black Hole. *ApJ*, 703(2):L142–L146.

Event Horizon Telescope Collaboration (2019). First M87 Event Horizon Telescope Results. I. The Shadow of the Supermassive Black Hole. *ApJ*, 875(1):L1.

Falcke, H. and Biermann, P. L. (1995). The jet-disk symbiosis. I. Radio to X-ray emission models for quasars. *A&A*, 293:665–682.

Falcke, H., Körding, E., and Markoff, S. (2004). A scheme to unify low-power accreting black holes. Jet-dominated accretion flows and the radio/X-ray correlation. *A&A*, 414:895–903.

Falcke, H., Melia, F., and Agol, E. (2000). Viewing the Shadow of the Black Hole at the Galactic Center. *ApJ*, 528:L13–L16.

Falcke, H., Nagar, N. M., Wilson, A. S., Ho, L. C., and Ulvestad, J. S. (2001). Radio Cores in Low-Luminosity AGN: ADAFs or Jets? In Kaper, L., Heuvel, E. P. J. V. D., and Woudt, P. A., editors, *Black Holes in Binaries and Galactic Nuclei*, page 218.

Gabuzda, D. C. and Cawthorne, T. V. (2000). VLBI polarization images of eight compact active galactic nuclei at λ=1.3cm. *MNRAS*, 319(4):1056–1066.

Gabuzda, D. C., Sitko, M. L., and Smith, P. S. (1996). Correlations Between the VLBI and Optical Polarization of BL Lacertae Objects. *AJ*, 112:1877.

Gammie, C. F. and Leung, P. K. (2012). A Formalism for Covariant Polarized Radiative Transport by Ray Tracing. *ApJ*, 752:123.

Gammie, C. F., McKinney, J. C., and Tóth, G. (2003). HARM: A Numerical Scheme for General Relativistic Magnetohydrodynamics. *ApJ*, 589:444–457.

Gautschi, W. (2011). *Numerical Analysis*. Birkhäuser Basel.

Goddi, C., Falcke, H., Kramer, M., Rezzolla, L., Brinkerink, C., Bronzwaer, T., Davelaar, J. R. J., Deane, R., de Laurentis, M., Desvignes, G., Eatough, R. P., Eisenhauer, F., Fraga-Encinas, R., Fromm, C. M., Gillessen, S., Grenzebach, A., Issaoun, S., Janßen, M., Konoplya, R., Krichbaum, T. P., Laing, R., Liu, K., Lu, R. S., Mizuno, Y., Moscibrodzka, M., Müller, C., Olivares, H., Pfuhl, O., Porth, O., Roelofs, F., Ros, E., Schuster, K., Tilanus, R., Torne, P., van Bemmel, I., van Langevelde, H. J., Wex, N., Younsi, Z., and Zhidenko, A. (2017). BlackHoleCam: Fundamental physics of the galactic center. *International Journal of Modern Physics D*, 26(2):1730001–239.

Gralla, S. E., Holz, D. E., and Wald, R. M. (2019). Black hole shadows, photon rings, and lensing rings. *Phys. Rev. D*, 100(2):024018.

Gravity Collaboration (2018). Detection of orbital motions near the last stable circular orbit of the massive black hole SgrA*. *A&A*, 618:L10.

Hada, K., Kino, M., Doi, A., Nagai, H., Honma, M., Akiyama, K., Tazaki, F., Lico, R., Giroletti, M., Giovannini, G., Orienti, M., and Hagiwara, Y. (2016). High-sensitivity 86 GHz (3.5 mm) VLBI Observations of M87: Deep Imaging of the Jet Base at a Resolution of 10 Schwarzschild Radii. *ApJ*, 817(2):131.

Hamaker, J. P. and Bregman, J. D. (1996). Understanding radio polarimetry. III. Interpreting the IAU/IEEE definitions of the Stokes parameters. *A&AS*, 117:161–165.

Heeschen, D. S. (1970). Radio Observations of E and SO Galaxies. *AJ*, 75:523–529.

Jaroszynski, M. and Kurpiewski, A. (1997). Optics near Kerr black holes: spectra of advection dominated accretion flows. *A&A*, 326:419–426.

Jiménez-Rosales, A. and Dexter, J. (2018). The impact of Faraday effects on polarized black hole images of Sagittarius A*. *MNRAS*, 478(2):1875–1883.

Johnson, M. D., Fish, V. L., and Doeleman, S. S. e. a. (2015). Resolved magnetic-field structure and variability near the event horizon of Sagittarius A*. *Science*, 350(6265):1242–1245.

Jones, T. W. and Hardee, P. E. (1979). Maxwellian synchrotron sources. *ApJ*, 228:268–278.

Landi Degl'Innocenti, E. and Landi Degl'Innocenti, M. (1985). On the solution of the radiative transfer equations for polarized radiation. *Sol. Phys.*, 97:239–250.

Lyutikov, M., Pariev, V. I., and Gabuzda, D. C. (2005). Polarization and structure of relativistic parsec-scale AGN jets. *MNRAS*, 360(3):869–891.

Misner, C. W., Thorne, K. S., and Wheeler, J. A. (1973). *Gravitation*.

Mizuno, Y., Younsi, Z., Fromm, C. M., Porth, O., De Laurentis, M., Olivares, H., Falcke, H., Kramer, M., and Rezzolla, L. (2018). The current ability to test theories of gravity with black hole shadows. *Nature Astronomy*, 2:585–590.

Mościbrodzka, M., Falcke, H., and Shiokawa, H. (2016). General relativistic magnetohydrodynamical simulations of the jet in M 87. *A&A*, 586:A38.

Moscibrodzka, M., Gammie, C., Dolence, J., Shiokawa, H., and Leung, P. (2009). Radiative Models of Sgr A* from GRMHD Simulations. In Wolk, S., Fruscione, A., and Swartz, D., editors, *Chandra's First Decade of Discovery*.

Moscibrodzka, M. and Gammie, C. F. (2017). ipole - semianalytic scheme for relativistic polarized radiative transport. *ArXiv e-prints*.

Narayan, R., Johnson, M. D., and Gammie, C. F. (2019). The Shadow of a Spherically Accreting Black Hole. *ApJ*, 885(2):L33.

Narayan, R., Mahadevan, R., and Quataert, E. (1998). Advection-dominated accretion around black holes. In Abramowicz, M. A., Björnsson, G., and Pringle, J. E., editors, *Theory of Black Hole Accretion Disks*, pages 148–182.

Noble, S. C., Leung, P. K., Gammie, C. F., and Book, L. G. (2007). Simulating the emission and outflows from accretion discs. *Classical and Quantum Gravity*, 24:259.

Novikov, I. D. and Thorne, K. S. (1973). Astrophysics of black holes. In Dewitt, C. and Dewitt, B. S., editors, *Black Holes (Les Astres Occlus)*, pages 343–450.

Palumbo, D. C. M., Wong, G. N., and Prather, B. S. (2020). Discriminating Accretion States via Rotational Symmetry in Simulated Polarimetric Images of M87. *arXiv e-prints*, page arXiv:2004.01751.

Rees, D. E., Murphy, G. A., and Durrant, C. J. (1989). Stokes Profile Analysis and Vector Magnetic Fields. II. Formal Numerical Solutions of the Stokes Transfer Equations. *ApJ*, 339:1093.

Schnittman, J. D. and Krolik, J. H. (2009). X-ray Polarization from Accreting Black Holes: The Thermal State. *ApJ*, 701(2):1175–1187.

Shakura, N. I. and Sunyaev, R. A. (1973). Reprint of 1973A&A....24..337S. Black holes in binary systems. Observational appearance. *A&A*, 500:33–51.

Shcherbakov, R. V. and Huang, L. (2011). General relativistic polarized radiative transfer: building a dynamics-observations interface. *MNRAS*, 410:1052–1063.

Wrobel, J. M. and Heeschen, D. S. (1991). Radio Continuum Sources in Nearby and Bright E/S0 Galaxies: Active Nuclei Versus Star Formation. *AJ*, 101:148.

Younsi, Z., Porth, O., Mizuno, Y., Fromm, C. M., and Olivares, H. (2020). Modelling the polarised emission from black holes on event horizon-scales. In Asada, K., de Gouveia Dal Pino, E., Giroletti, M., Nagai, H., and Nemmen, R., editors, *IAU Symposium*, volume 342 of *IAU Symposium*, pages 9–12.

Younsi, Z., Wu, K., and Fuerst, S. V. (2012). General relativistic radiative transfer: formulation and emission from structured tori around black holes. *A&A*, 545:A13.

Yuan, F., Quataert, E., and Narayan, R. (2003). Nonthermal Electrons in Radiatively Inefficient Accretion Flow Models of Sagittarius A*. *ApJ*, 598(1):301–312.

Appendix A: Stiffness analysis of the polarized radiative-transfer equation

The stiffness of a linear system of differential equations, such as the polarized radiative-transfer equation (Eq. 12), with respect to a particular explicit integration scheme (such as the fourth-order Runge-Kutta integrator used here), depends on the eigenvalues of the matrix which appears on that equation's right-hand side, $\mathbf{M}$; our first step is to compute them.

In a frame in which $j_U = \alpha_U = \rho_U = 0$, $\mathbf{M}$'s characteristic polynomial is given by

$$|\mathbf{M}| = z^2 + a_2 z + a_0 = 0, \tag{A.1}$$

where

$$z = (\alpha_I - \Lambda)^2, \tag{A.2a}$$
$$a_2 = \rho_Q^2 + \rho_V^2 - \alpha_Q^2 - \alpha_V^2, \tag{A.2b}$$
$$a_0 = -2\alpha_Q\alpha_V\rho_Q\rho_V - \alpha_Q^2\rho_Q^2 - \alpha_V^2\rho_V^2, \tag{A.2c}$$

Λ being an eigenvalue of $\mathbf{M}$. In other words, $\mathbf{M}$'s characteristic polynomial is a biquadratic equation in $(\alpha_I - \Lambda)$, which may therefore be obtained by solving the quadratic equation:

$$z_\pm = \frac{-a_2 \pm \sqrt{a_2^2 - 4a_0}}{2}. \tag{A.3}$$

There are then four possible values for $(\alpha_I - \Lambda)$:

$$(\alpha_I - \Lambda) = \begin{cases} +\sqrt{z_+}, \\ -\sqrt{z_+}, \\ +\sqrt{z_-}, \\ -\sqrt{z_-}, \end{cases} \tag{A.4a}$$

so that

$$\Lambda = \alpha_I \pm \sqrt{z_\pm}, \tag{A.5}$$

where either plus/minus symbol may be interpreted in either way.

Now that $\mathbf{M}$'s eigenvalues are known, the stiffness of Eq. 12 for the explicit fourth-order Runge-Kutta integrator can be computed. Defining

$$\zeta = \Delta\lambda\Lambda, \tag{A.6}$$

where $\Delta\lambda$ is `RAPTOR`'s integration step size, the explicit fourth-order Runge-Kutta integration routine is stable when

$$\left|1 + \zeta + \frac{1}{2}\zeta^2 + \frac{1}{6}\zeta^3 + \frac{1}{24}\zeta^4\right| < 1. \tag{A.7}$$

Whenever this condition is not met for any one of $\mathbf{M}$'s four eigenvalues, it is necessary to switch to the implicit trapezoid integration routine.

Appendix B: Implicit trapezoid integrator

Rewriting Eq. 15, we obtain a system of equations for $\boldsymbol{\mathcal{S}}_{new}$:

$$\underbrace{\left(\mathbb{1} + \frac{\Delta\lambda}{2}\mathbf{M}\right)}_{\mathbf{A}}\boldsymbol{\mathcal{S}}_{new} = \underbrace{\boldsymbol{\mathcal{S}} + \frac{\Delta\lambda}{2}\left(2\mathbf{j} - \mathbf{M}\boldsymbol{\mathcal{S}}\right)}_{\mathbf{b}}. \tag{B.1}$$

The matrix $\mathbf{A}$, evaluated in a frame in which j_U, α_U, and ρ_U vanish, is then given by

$$\mathbf{A} = \begin{pmatrix} 1 + \Delta\lambda\alpha_I/2 & \Delta\lambda\alpha_Q/2 & 0 & \Delta\lambda\alpha_V/2 \\ \Delta\lambda\alpha_Q/2 & 1 + \Delta\lambda\alpha_I/2 & \Delta\lambda\rho_V/2 & 0 \\ 0 & -\Delta\lambda\rho_V/2 & 1 + \Delta\lambda\alpha_I/2 & \Delta\lambda\rho_Q/2 \\ \Delta\lambda\alpha_V/2 & 0 & -\Delta\lambda\rho_Q/2 & 1 + \Delta\lambda\alpha_I/2 \end{pmatrix}. \tag{B.2}$$

Next, we express $\mathbf{A}$ as a product of two triangular matrixes, $\mathbf{L}$ and $\mathbf{U}$:

$$\mathbf{A} = \mathbf{LU} = \begin{pmatrix} 1 & 0 & 0 & 0 \\ l_{21} & 1 & 0 & 0 \\ l_{31} & l_{32} & 1 & 0 \\ l_{41} & l_{42} & l_{43} & 1 \end{pmatrix}\begin{pmatrix} u_{11} & u_{12} & u_{13} & u_{14} \\ 0 & u_{22} & u_{23} & u_{24} \\ 0 & 0 & u_{33} & u_{34} \\ 0 & 0 & 0 & u_{44} \end{pmatrix}, \tag{B.3}$$

whose elements are given by

$$u_{11} = 1 + \Delta\lambda\alpha_I/2, \tag{B.4a}$$
$$u_{12} = \Delta\lambda\alpha_Q/2, \tag{B.4b}$$
$$u_{13} = 0, \tag{B.4c}$$
$$u_{14} = \Delta\lambda\alpha_V/2, \tag{B.4d}$$
$$l_{21} = \frac{\Delta\lambda\alpha_Q}{2u_{11}}, \tag{B.4e}$$
$$u_{22} = 1 + \Delta\lambda\alpha_I/2 - l_{21}u_{12}, \tag{B.4f}$$
$$u_{23} = \Delta\lambda\rho_V/2, \tag{B.4g}$$
$$u_{24} = -l_{21}u_{14}, \tag{B.4h}$$
$$l_{31} = 0, \tag{B.4i}$$
$$l_{32} = -\frac{\Delta\lambda\rho_V}{2u_{22}}, \tag{B.4j}$$
$$u_{33} = 1 + \Delta\lambda\alpha_I/2 - l_{32}u_{23}, \tag{B.4k}$$
$$u_{34} = \Delta\lambda\rho_Q/2 - l_{32}u_{24}, \tag{B.4l}$$
$$l_{41} = \frac{\Delta\lambda\alpha_V}{2u_1 1}, \tag{B.4m}$$
$$l_{42} = -\frac{l_{41}u_{12}}{u_{22}}, \tag{B.4n}$$
$$l_{43} = -\frac{\Delta\lambda\rho_Q/2 + l_{42}u_{23}}{u_{33}}, \tag{B.4o}$$
$$u_{44} = 1 + \Delta\lambda\alpha_I/2 - l_{41}u_{14} - l_{42}u_{24} - l_{43}u_{34}. \tag{B.4p}$$

This allows us to obtain $\boldsymbol{\mathcal{S}}_{new}$ explicitly, from two linear systems of equations:

$$\mathbf{Ly} = \mathbf{b}, \tag{B.5a}$$
$$\mathbf{U}\boldsymbol{\mathcal{S}}_{new} = \mathbf{y}, \tag{B.5b}$$

where $\mathbf{y}$'s components are given by

$$y_1 = b_1, \tag{B.6a}$$
$$y_2 = b_2 - l_{21}y_1, \tag{B.6b}$$
$$y_3 = b_3 - l_{32}y_2, \tag{B.6c}$$
$$y_4 = b_4 - (l_{41}y_1 + l_{42}y_2 + l_{43}y_3). \tag{B.6d}$$

$\mathcal{S}_{new}$ is then computed as follows:

$$\mathcal{S}_{new,1} = \frac{y_1 - u_{12}x_2 - u_{14}x_4}{u_{11}}, \tag{B.7a}$$

$$\mathcal{S}_{new,2} = \frac{y_2 - u_{23}x_3 - u_{24}x_4}{u_{22}}, \tag{B.7b}$$

$$\mathcal{S}_{new,3} = \frac{y_3 - u_{34}x_4}{u_{33}}, \tag{B.7c}$$

$$\mathcal{S}_{new,4} = \frac{y_4}{u_{44}}. \tag{B.7d}$$

Appendix C: Emission, absorption, and rotation coefficients for a thermal electron population

This appendix lists the emission, absorption, and rotation coefficients employed in RAPTOR. They pertain to a (relativistic) thermal distribution of electrons. They are adapted from Dexter (2016) (note that non-thermal (power-law) coefficients are also listed in that paper), with a number of modifications of numerical fit functions by Moscibrodzka and Gammie (2017), as well as minor notational rewrites in eqs. C.6 and typographical corrections in eq. **??** (cf. B14 in Dexter (2016)).

The emission coefficients are given by

$$j_I = \frac{n_e e^2 \nu}{2\sqrt{3} c {\theta_e}^2} I_I(x), \tag{C.1a}$$

$$j_Q = \frac{n_e e^2 \nu}{2\sqrt{3} c {\theta_e}^2} I_Q(x), \tag{C.1b}$$

$$j_V = \frac{2 n_e e^2 \nu}{3\sqrt{3} c {\theta_e}^3 \tan\theta_B} I_V(x), \tag{C.1c}$$

where n_e is the electron number density, e is the electron charge, c is the speed of light, θ_e is the dimensionless electron temperature, θ_B is the angle between the wave vector and the magnetic-field vector, and x is the ratio of the ray's frequency over the critical plasma frequency:

$$x = \frac{\nu}{\nu_c}, \tag{C.2}$$

where

$$\nu_c = \frac{3eB\sin\theta_B \theta_e^2}{4\pi m_e c}, \tag{C.3}$$

with B being the magnetic-field amplitude (in Gaussian-cgs units).

The expressions I_I, I_Q, I_V represent numerical fit functions, and are given by

$$I_I(x) = 2.5651\left(1 + 1.92x^{-1/3} + 0.9977x^{-2/3}\right)e^{-1.8899x^{1/3}}, \tag{C.4a}$$

$$I_Q(x) = 2.5651\left(1 + 0.93193x^{-1/3} + 0.499873x^{-2/3}\right)e^{-1.8899x^{1/3}}, \tag{C.4b}$$

$$I_V(x) = (1.81348/x + 3.42319x^{-2/3} + 0.0292545x^{-1/2} + 2.03773x^{-1/3})e^{-1.8899x^{1/3}}. \tag{C.4c}$$

Absorption is computed using Kirchoff's law, as the distribution is thermal, so that the absorption coefficients may be written as

$$\alpha_\nu = j_\nu / B_\nu, \tag{C.5}$$

where B_ν is the blackbody function.

Finally, the rotation coefficients are given by

$$\rho_Q = \frac{\omega_p^2 \omega_0^2 \sin^2\theta_B}{16 c \pi^3 \nu^3} f_m\left(\tilde{X}\right) + \left[\frac{K_1\left(\theta_e^{-1}\right)}{K_2\left(\theta_e^{-1}\right)} + 6\theta_e\right], \tag{C.6a}$$

$$\rho_V = \frac{\omega_p^2 \omega_0 \cos\theta_B}{4 c \pi^2 \nu^2} \frac{K_0\left(\theta_e^{-1}\right) - \Delta J_5\left(\tilde{X}\right)}{K_2\left(\theta_e^{-1}\right)}, \tag{C.6b}$$

where

$$\omega_p^2 = 4\pi n_e e^2 / m_e, \tag{C.7}$$

$$\tilde{X} = \left(\frac{3}{2\sqrt{2}} 10^{-3} \frac{\nu}{\nu_c} \right)^{-1/2}, \tag{C.8}$$

and

$$\omega_0 = \frac{eB}{m_e c}. \tag{C.9}$$

The functions f_m and ΔJ_5 again represent fit functions. They are given by

$$f_m\left(\tilde{X}\right) = 2.011 \exp\left(-\frac{\tilde{X}^{1.035}}{4.7}\right) - \cos\left(\frac{\tilde{X}}{2}\right) \exp\left(-\frac{\tilde{X}^{1.2}}{2.73}\right) - 0.011 \exp\left(-\frac{\tilde{X}}{47.2}\right) + \left(0.011 \exp\left(-\frac{\tilde{X}}{47.2}\right) - 2^{-1/3} 3^{-23/6} \pi 10^4 \tilde{X}^{-8/3}\right) \frac{1}{2} \left(1 + \frac{\tanh\left(\log \tilde{X} - \log 120\right)}{0.1}\right)$$

and

$$\Delta J_5\left(\tilde{X}\right) = 0.4379 \log\left(1 + 0.001858 \tilde{X}^{1.503}\right), \tag{C.10}$$

respectively.

Note that during a `RAPTOR` run, the Lorentz-invariant versions of these coefficients are employed. Transforming the emission, absorption, and rotation coefficients to their Lorentz-invariant forms proceeds as follows:

$$j_{\text{inv}} = j/\nu^2, \tag{C.11a}$$
$$\alpha_{\text{inv}} = \alpha\nu, \tag{C.11b}$$
$$\rho_{\text{inv}} = \rho\nu. \tag{C.11c}$$